Research Article

Mohammed H. Aljahdali and Mohamed Elhag*

Calibration of the depth invariant algorithm to monitor the tidal action of Rabigh City at the Red Sea Coast, Saudi Arabia

https://doi.org/10.1515/geo-2020-0217
received June 19, 2020; accepted November 30, 2020

Abstract: Rabigh is a thriving coastal city located at the eastern bank of the Red Sea, Saudi Arabia. The city has suffered from shoreline destruction because of the invasive tidal action powered principally by the wind speed and direction over shallow waters. This study was carried out to calibrate the water column depth in the vicinity of Rabigh. Optical and microwave remote sensing data from the European Space Agency were collected over 2 years (2017–2018) along with the analog daily monitoring of tidal data collected from the marine station of Rabigh. Depth invariant index (DII) was implemented utilizing the optical data, while the Wind Field Estimation algorithm was implemented utilizing the microwave data. The findings of the current research emphasis on the oscillation behavior of the depth invariant mean values and the mean astronomical tides resulted in R^2 of 0.75 and 0.79, respectively. Robust linear regression was established between the astronomical tide and the mean values of the normalized DII ($R^2 = 0.81$). The findings also indicated that January had the strongest wind speed solidly correlated with the depth invariant values ($R^2 = 0.92$). Therefore, decision-makers can depend on remote sensing data as an efficient tool to monitor natural phenomena and also to regulate human activities in fragile ecosystems.

Keywords: astronomical tide, bathymetry, regression coefficient, water column, wind speed

*** Corresponding author: Mohamed Elhag,** Department of Hydrology and Water Resources Management, Faculty of Meteorology, Environment and Arid Land Agriculture, King Abdulaziz University, Jeddah 21589, Saudi Arabia; Institute of Remote Sensing and Digital Earth (RADI), Chinese Academy of Science (CAS), Beijing 100094, China; Department of Applied Geosciences, Faculty of Science, German University of Technology in Oman, Muscat 1816, Oman, e-mail: melhag@kau.edu.sa
Mohammed H. Aljahdali: Marine Geology Department, Faculty of Marine Sciences, King Abdulaziz University, P.O. Box 80200, Jeddah 21589, Saudi Arabia

1 Introduction

Satellite and airborne remote sensing have become a common tool in the analysis of different fields in earth and environmental sciences. This science has improved the capability of acquiring information about the Earth and its resources for global, regional, and local assessments [1,2]. Many remote sensing studies have used multispectral remotely sensed imagery to provide consequential data, which prove to be a valuable source of spatiotemporal data for several applications [3,4].

Optical remote sensing data were used extensively over the past four decades in various applications of Earth observation and natural resources management studies. The most implemented techniques are the Land Use Land Cover classification algorithms [5,6], the estimation and the realization of the vegetation indices [7–10], and the monitoring and the assessment of the natural hazardousness [11,12].

Conversely, microwave remote sensing data were recently incorporated with different natural phenomena where the weather condition limits the application of the optical data [13]. Most of the microwave remote sensing data were used in studies concerning oil spill detection [14,15], land subsidence and seismic activities [16,17], urban coherence, and anomaly detection [18,19]. Recently, there was a development of algorithms that concerns the water column depth [20–22] and finally the wind speed and the direction at the water surface [23–25].

Tides are caused by the physics of the solar system and by the relative movements of the Earth, Sun, and Moon. Tides are recorded as changes in the water level and are associated with water motions called tidal currents [26,27]. Although technically called tidal streams since causes of ocean currents include meteorological forcing and density variations, most mariners use the term “tidal current” for the astronomical component as well [28,29].

The estimation algorithm of the water depth column was initially practiced by Platt [30], and then, it was

improved by Stumpf et al. [31] and Kerr and Purkis [32]. The algorithm takes into consideration the principles of the Electromagnetic Radiation (EMR) through the water bodies. Therefore, the depth of the water column and/or the quality of the examined water plays a fundamental role in the algorithm resulting [33,34]. Consequently, clear shallow waters would be ideal to conduct reliable water depth estimations [34]. Although the water depth estimations are EMR wavelength-dependent since shorter wavelengths (e.g., the Blue and the Green band of Sentinel-2) are the optimal wavelengths to interact with water bodies [30,34].

Remote sensing applications on shallow waters mapping aids the understanding of the nearshore habitats including corals bleaching and water column corrections [21,34]. Spectral signatures collected from the seabed that was necessary to comprehend the water column depth throughout an empirical model of Lyzenga [35]. The model was continuously improved to become widely implemented known as depth invariant index (DII). DII is a transformation semi-empirical model that uses the water spectral signatures to contemplate the water column attenuation [36–38].

The ideal estimation of the water depth column would be at a steady water surface with no wind interactions [39,40]. In addition, this condition does not represent the reality where water bodies are continuously affected by wind action, especially at the surfaces [41,42]. Accordingly, the estimation of surface roughness becomes an essential parameter to realize and to validate throughout the estimation of the water depth column [34]. Hence, the surface and the seabed roughness's are estimated consistently along with the swell structure, and the latter is correlated with the wind speed, wind direction, and the mud content [43,44].

The comprehensive objective of this study is to examine the effect of the tidal action on the water depth column near the shorelines of Rabigh. Correspondingly, the objective draws attention to tidal monitoring, water column calibration, and wind field estimation functions. Regression analysis was subsequently performed using the tide calendar data against the passive and active originated remote sensing data.

2 Materials and methods

2.1 Study area description

Rabigh is one of the Saudi coastal cities located on the Eastern side of the Red Sea at 22°44′03″N and 38°59′43″E (Figure 1). It is about ~160 km north of Jeddah and parallelly surrounded in the north by one of the largest lagoons in the Red Sea. The lagoon, formerly known as Al-Kharrar, is located 10 km northwest of Rabigh [45]. Al-Kharrar lagoon lies under dry and warm tropical climate where at several seasons evaporation exceeds the rates of precipitation, except between May and November when large input of freshwater delivered via wadis is discharged to the southern part of the basin [45,46]. Geological investigations suggest that the lagoon was formed mainly by a major drop in the sea level, and consequently

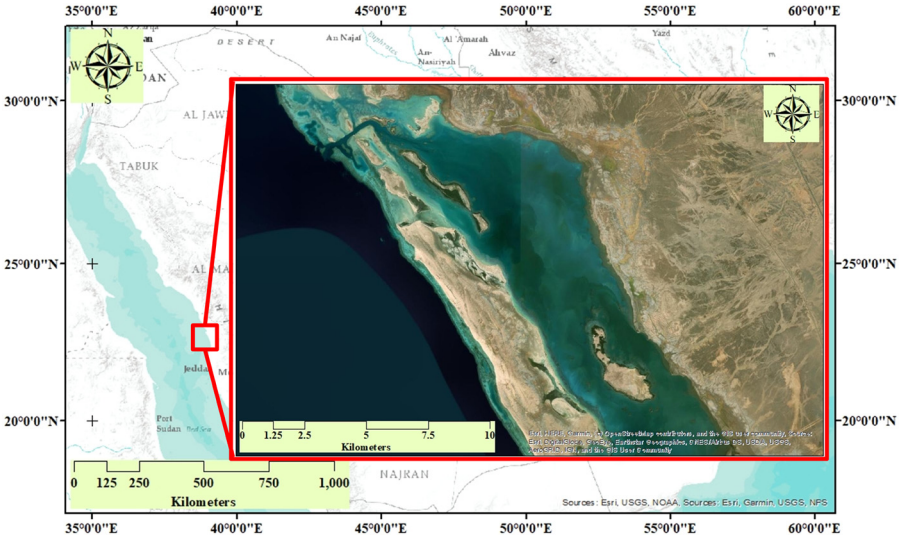

Figure 1: The location of the study area shows Al Khara lagoon of Rabigh.

erosion occurred in the late Pleistocene [47–49]. The open normal water characterized by 25°C temperature and 39 PSU salinity inflows through the inlet as surface current, while the lagoon hypersaline water characterized by 30°C temperature and 40 PSU salinity outflows toward the open water [45]. The mean annual wind speed of the designated study area is 10.6 m/s directed North and Northeast; furthermore, the sediment load covers about 1,270 km^2 annually for the city shoreline overdriven by flashfloods take place at the surrounding wadies [50].

2.2 Tidal monitoring

The time used in tidal data collection is the Coordinated Universal Time plus 3 h to match the actual local time. The calendar format for the Tide Calendar graphs begins with Sunday as the first day of the week. The Tidal data were collected from the Saudi Aramco station and referenced to Lowest Astronomical Tide (LAT). LAT is calculated and is defined as the "lowest level that can occur under average meteorological conditions and any combination of astronomical conditions." It should be realized that "abnormal" weather conditions (e.g., high barometric pressures and strong offshore winds) can lower values below LAT [51].

2.3 Remote sensing data

Two data sets of remote sensing data in the form of optical and microwave data were collected monthly from the European Space Agency (ESA) freely access catalog starting from January 2017 until December 2018. The optical data were conducted from Sentenial-2A instrumental, Multi-Spectral Instrument (MSI). While the Microwave data were collected from Sentinel-1B, Ground Range Detected (GRD) designed to register the C-band (5.546 cm wavelength) in 20 m spatial resolution.

2.4 Conceptual framework

2.4.1 Resampling

The MSI on-board Sentinel-2 composed of bands does not have the same spatial resolution. Visible bands and B8 (B2, B3, and B4) are registered in 10 m, and infrared (IR) and shortwave infrared (SWIR) bands (B5, B6, B7, B8a, B11, and B12) are registered in 20 m, while the cloud screen and aerosol bands (B1, B9, and B10) are registered in 60 m spatial resolution. The bands that are most sensitive to surface water reflection are B2 and B3, and radiated wavelengths off water bodies need to be calibrated using the radiated wavelengths of B8 and B9 [52], and because these bands are in different spatial resolution, data resampling preferably to B2 is a mandatory procedure in water column calibration [34,53].

2.4.2 Radiometric and atmospheric corrections

Temporal data analysis demonstrates radiometric distortion due to data acquisition atmospheric variabilities. Consequently, radiometric normalization to imagery is required, so the values corresponding to the same surface become comparable throughout temporal analyses [54,55]. The histogram normalization method is based on the use of pseudo-invariant features (PIFs) corresponding to optically bright targets (infrastructures) or optically dark targets (deep waters) to intercalibrate different images radiometrically [56,57].

The used data sets in the current research study are atmospherically corrected images (L2A-level), which means that the reflectance values of the bottom-of-atmosphere (BOA) from the top-of-atmosphere (TOA) reflectances are corrected by eliminating the atmospheric interactions [58,59]. The implementation of the bathymetry algorithm for the Sentinel-2 product performs the atmospheric, terrain, and cirrus correction of the TOA input data. The algorithm creates BOA additional with the terrain and the cirrus-corrected reflectance images [60,61].

2.4.3 Deglint

The specular reflection of the sun radiations off water surfaces creates a frequent phenomenon known as "sun glint" in remote sensing images. Glint reflections do not penetrate the water surface and do not draw any spectral information about water subsurfaces [62]. Thus, the water-leaving reflectances are hard to monitor due to the nadir reflection of sun radiations on the air–water surfaces [63]. Therefore, the algorithm of glint removal (deglint) is performed to improve the seafloor mapping [37,64]. In principle, the algorithm performs linear regressions between NIR brightness represented by the x-axis and the band reflectance represented by the y-axis using

the predefined ROI's for deep water surfaces when it is expected to be ideally homogeneous (Figure 2). The gradient of the regression line is the quest of significance for given band i (bi). According to Hedley et al. [65,66], the algorithm was performed as follows:

$$R_i' = R_i - b_i\,(R_{\mathrm{NIR}} - \mathrm{Min}_{\mathrm{NIR}}), \tag{1}$$

where NIR is the near infrared band of Sentinel 2.

2.4.4 Land/water mask

To avoid interference with land surface reflectance, an additional task is performed to mask the land/water surfaces. Masking of the bright objects (land surfaces) is mandatory since the water bodies do not allow the near infrared (NIR) wavelengths to penetrate [67]. Accordingly, water bodies appear dark in the satellite images following the deglint processor performance using the proper masking threshold [67,68].

2.4.5 Depth invariant indices

The fundamental concept of the depth invariant algorithm is based on the water bodies' reflectance that is exponentially inverted with water bodies' depth in approximation. According to Philpot [69] and Poursanidis et al. [70], the linearization of the deepwater reflectances shall be carried out as follows:

$$X_i = \ln\,(R_i - R_i^{\mathrm{deep}}), \tag{2}$$

where R_i is Sentinel-2 band "i" reflectance and R_i^{deep} is Sentinel-2 band "i" deep reflectance.

Usually, bands 2 and 3 are most commonly used for the depth invariant algorithm, sand, vegetation, and mud slopes behavior plotted against those 2 bands that are the same although the intercepts of these objects to the plotting axes are different [38,71]. This empirical function can be performed as follows:

$$X_i = \frac{K_i}{K_j} X_j + d_{ij}, \tag{3}$$

where d_{ij} is the intercept constant of the questioned DII. K_i/K_j is the water reflectance attenuation coefficient.

Therefore, it is necessary to identify two different depths of the water bodies within the satellite footage to represent the shallow and the deepwater surfaces (Figure 3). A total of 10 depth samples were collected from the Lagoon to represent the shallow waters, and another 10 depth samples were collected from the open sea to represent deep waters (Table 1). The differentiation between shallow and depth waters was based on the naked eye reef visibility [72]. Consequently, the attenuation reflectances of variant water surfaces are estimated according to the perpendicular offset's method of Sordillo et al. [67] as follows:

$$K_i/K_j = a + \sqrt{a^2 + 1}\,, \tag{4}$$

where

$$a = \frac{\sigma_{ii} - \sigma_{jj}}{2\sigma_{ij}}. \tag{5}$$

Then,

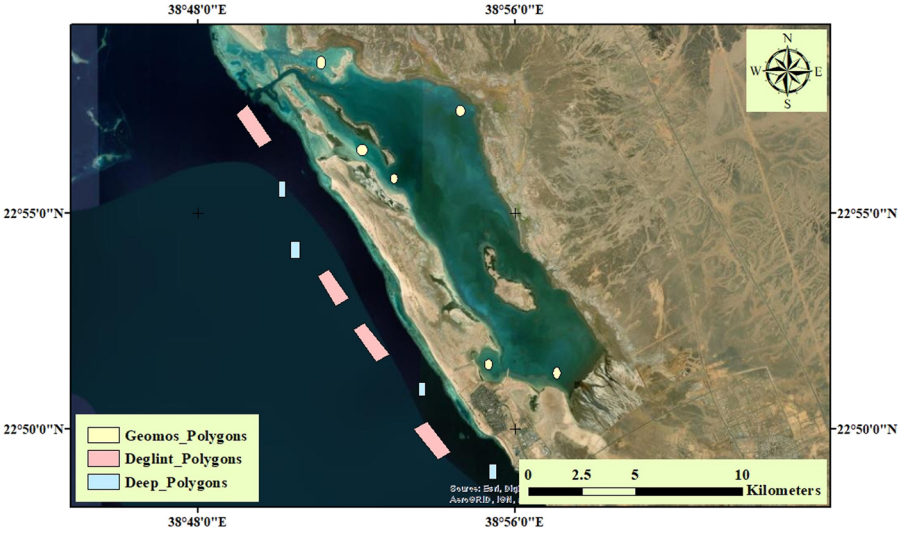

Figure 2: ROI's for deep, shallow water, and deglint.

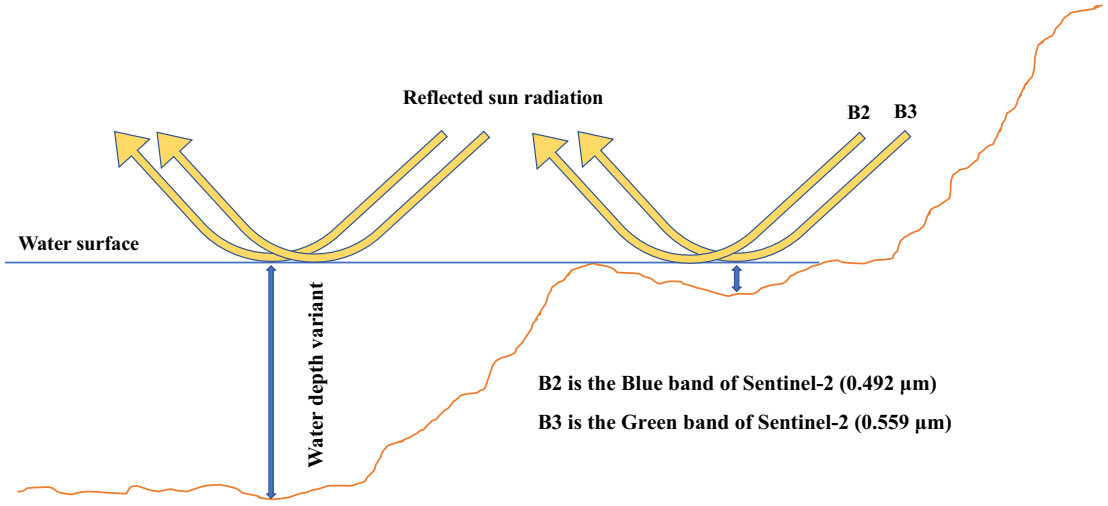

Figure 3: Depth invariant concept.

$$\sigma_{ij} = \overline{X_i - X_j} - (\overline{X_i} - \overline{X_j}). \quad (6)$$

Decisively, the DII is estimated according to Poursanidis et al. [70] as follows:

$$d_{ij} = X_i - \frac{K_i}{K_j} X_j. \quad (7)$$

Wind speed and wind direction affect systematically the wave intensity especially in shallow waters where the wind speed and the current speed are relatively the same. Furthermore, tidal action affects proportionally the onshore water column [22,30]. Microwave data fashioned in the C-band obtained from Sentinel-1 significantly enhanced the wind estimation remotely. The algorithm developed by Lehner et al. [73] and Yijun He et al. [74] detects the water surface roughness in terms of speed and direction using the Geophysical Model Function (GMF) of CMOD-5. The GMF was initially developed by Stoffelen and Anderson [75] and written as follows:

$$Z^m(\upsilon, \phi, \theta) = B0^p(\upsilon, \theta)\{1 + B1(\upsilon, \theta)\cos(\phi) + B2(\upsilon, \theta)\cos(2\phi)\}. \quad (8)$$

Table 1: Location and the depth (m) of the water depth samples

Pin id	Pin X coordinate (north)	Pin Y coordinate (east)	Depth (m)	
1	22°59′12.45″N	38°49′57.96″E	0.33	Lagoon samples
2	22°58′38.50″N	38°51′22.82″E	0.28	
3	22°57′50.10″N	38°50′51.49″E	0.56	
4	22°56′23.51″N	38°52′23.72″E	0.47	
5	22°56′19.30″N	38°54′13.40″E	0.84	
6	22°54′45.90″N	38°53′47.59″E	0.68	
7	22°54′6.85″N	38°55′56.58″E	0.59	
8	22°51′53.59″N	38°55′44.57″E	0.63	
9	22°51′19.63″N	38°56′9.44″E	0.58	
10	22°51′52.69″N	38°57′41.59″E	0.69	
11	22°58′44.87″N	38°47′49.62″E	5.30	Open water samples
12	22°57′11.84″N	38°49′49.80″E	8.12	
13	22°55′34.24″N	38°50′51.59″E	9.54	
14	22°54′2.60″N	38°51′52.44″E	7.98	
15	22°52′32.63″N	38°52′47.73″E	11.57	
16	22°51′17.08″N	38°53′38.42″E	12.41	
17	22°50′38.97″N	38°54′8.12″E	6.52	
18	22°49′25.12″N	38°55′18.12″E	8.34	
19	22°53′38.99″N	38°51′37.95″E	10.84	
20	22°51′7.83″N	38°53′26.67″E	12.00	

where

$$\varphi = \chi - \alpha,$$

Then,

$$z = \sigma_0^p,$$

where α is the azimuth angle, χ is the wind direction, v is the wind speed, θ is the incident angle, $B0$ is the wind speed and incidence angle coefficient, $B1$ is the upwind/downwind effects, $B2$ is the unwind/crosswind effects, and P is the transformed coefficient ($p = 0.625$).

The CMOD-5 model is designed for the Normalized Radar Cross Section (NRCS). The model converts the NRCS-HH into NRCS-VV polarization according to Lehner et al. [73] and written as follows:

$$\sigma_v^0 = \frac{(1 + 2\tan^2(\theta))^2}{(1 + \alpha\tan^2(\theta))^2}\,\sigma_H^0 \tag{9}$$

where α is set to 1 and H is the horizontal polarization.

The microwave data were preprocessed to ensure the precise orbit file identification, the Thermal Noise Removal-processor according to Park et al. [76] and finally the GRD Border Noise Removal according to Ali et al. [77]. The overall framework is demonstrated in Figure 4.

3 Results and discussion

The integration of the remote sensing data analysis was conducted to understand the relationship between the shallow water surfaces and the EMR. Regression analysis was practiced evaluating the regression coefficient under different data settings (maximum, minimum, and mean values).

Normalized DII mean values (>4) were found within November 2017 and April and July 2018, whereas lower values were distributed within March to September and late October 2017 and February 2018 (Figure 5). Overall, a goodness-of-fit R^2 shows a positive correlation between the mean DII and the designated timeframe. Moreover, DII values showed a typical oscillation between November 2017 and February 2018 covering four astronomical seasons (Spring, Autumn, Winter, and Summer) in which the index ranges between 1 and 5 (Figure 6).

The mean astronomical tide (in cm) values show unequivocal oscillation between November 2017 and February 2018 in which they ranged between 20 and ~50 cm (Figure 7). The highest (rise) mean astronomical tide values were found in November 2017 and October 2018, mainly characterized by the tidal rise of about 46 and 48 cm, respectively. The lowest (retreat) mean values, however, were found within September and December 2017 and up to April 2018. The relationship between mean astronomical tide (cm) and our timeframe is quite positive with a coefficient of determination, i.e., $R^2 = 0.79$.

The maximum DII values versus the designated studied astronomical timeframe show a slight fluctuation between November 2017 and February 2018 in which the maximum DII values are within the range between 6 and 11 (Figure 8). The fluctuation pattern of the maximum DII matches the mean DII data that are characterized by a trough (higher values) between September and

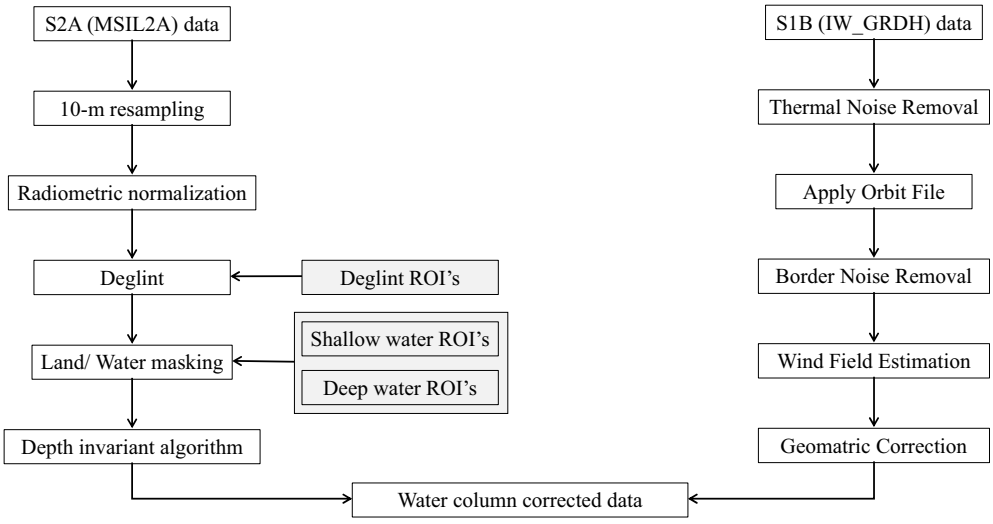

Figure 4: Depth invariant conceptual framework.

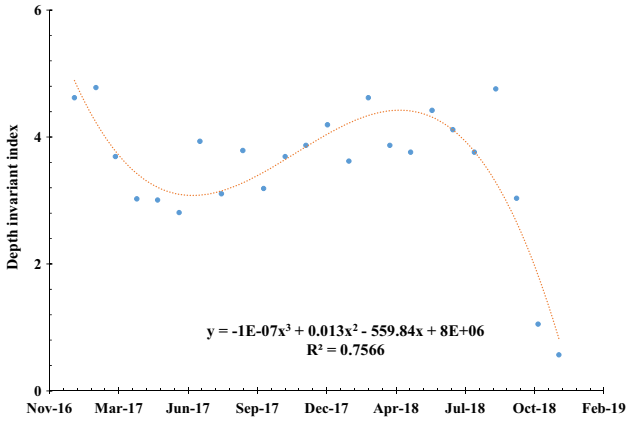

Figure 5: Distribution of the mean values of the DII.

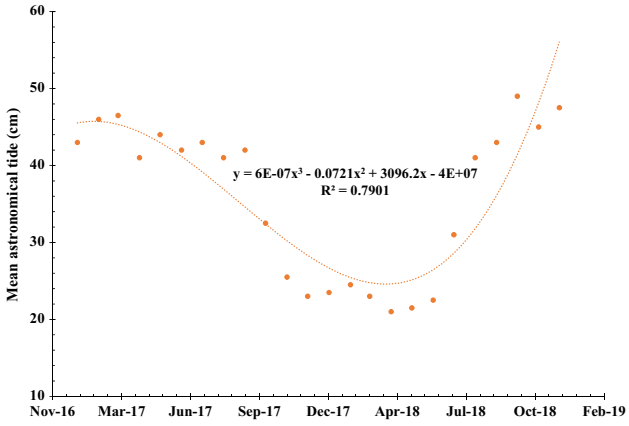

Figure 6: Distribution of the mean values of the astronomical tide (cm).

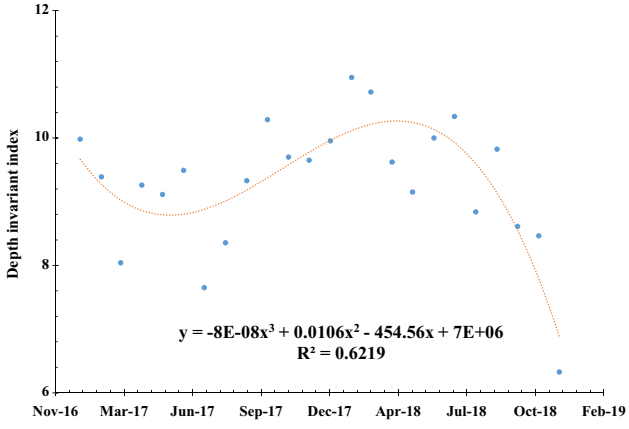

Figure 7: Distribution of the maximum values of the DII.

December 2017, and April 2018. The lowest values in the maximum DII are also incomparable with the mean DII (see Figure 6) and the R^2 = 0.6, suggesting a slight

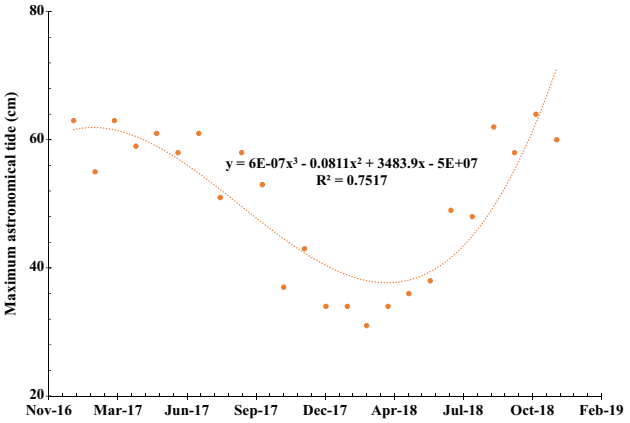

Figure 8: Distribution of the maximum values of the astronomical tide (cm).

positive correlation between the maximum DII and timeframe.

The maximum values of the astronomical tide (cm) show a clear oscillation resembling the mean astronomical tide in Figure 7, in which the maximum values range between 30 and 70 cm (Figure 9). The highest maximum values are concentrated around November 2017 and June 2018, and October 2017 and February 2018, while the lowest values are found to characterize the months of September 2017 and July 2018 (Figure 9). The coefficient of determination R^2 was calculated to be 0.752 between the maximum astronomical tide (cm) and months, which suggests a reasonably positive correlation.

The minimum DII values show a clear oscillation/fluctuation between November 2017 and February 2018 with values ranging between 0.9 and 1.5 (Figure 10). The channel that represents the highest values of the minimum DII is found between December 2017 and April and July 2018. As similar to the DII mean and maximum data (Figures 6 and 8), the coefficient of determination R^2 is 0.75, suggesting a positive correlation reminiscent of the mean and max DII correlation with the timeframe.

The minimum astronomical tide values show a similar fluctuation pattern reminiscent of the mean and maximum astronomical tide between November 2017 and February 2018 (Figure 10). The values range between 8 and 40 cm, and the months between November 2017 and June and July 2018 and February 2019 represent a high rise in tide. The high tidal values range between >20 and >40 cm, whereas the lowest tide retreat values are found to clump within 8–10 cm. Parallel to the mean and max astronomical tide (cm) illustrated in Figures 6 and 8, the correlation coefficient R^2 is 0.60, which suggests a weak correlation.

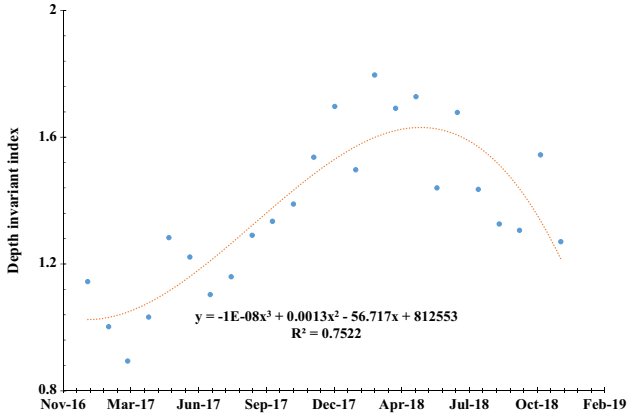

Figure 9: Distribution of the minimum values of the DII.

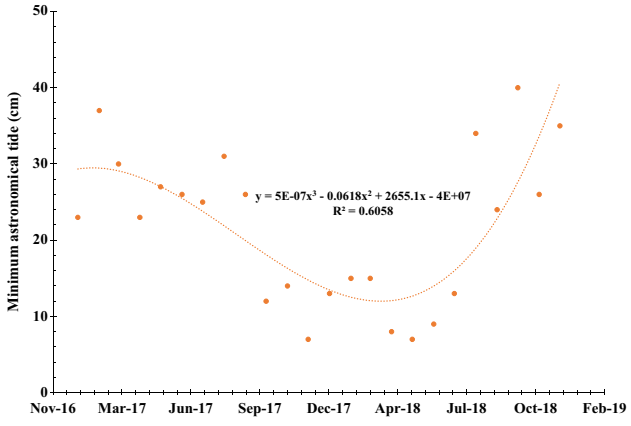

Figure 10: Distribution of the minimum values of the astronomical tide (cm).

The correlation coefficient of the normalized mean, max, and min tidal values versus remotely sensed depth shows a strong positive correlation (Figures 11–13). All estimated and actual values suggest a strong positive correlation with depth.

The DII values of January (2017/2018) range between 0 and 6, while the wind speed values (m/s) range between 0.1 and 9.4 m/s (Figure 14) with an average wind speed of 3.8 m/s during January. The highest value of the DII (6.6) corresponds to a wind speed of about 9.4 m/s. In general, there is a clear trend of increasing DII values with the increase of wind speed, in which R^2 = 0.92 suggests a positive correlation.

The DII values of April (2017/2018) range between 0 and 7, while the wind speed values (m/s) range between 0.1 and 5.4 m/s (Figure 15) with an average wind speed of 2.2 m/s during April. The highest value of the DII (7.3) corresponds to a wind speed of about 3.5 m/s. There is no clear trend of such a positive correlation between the

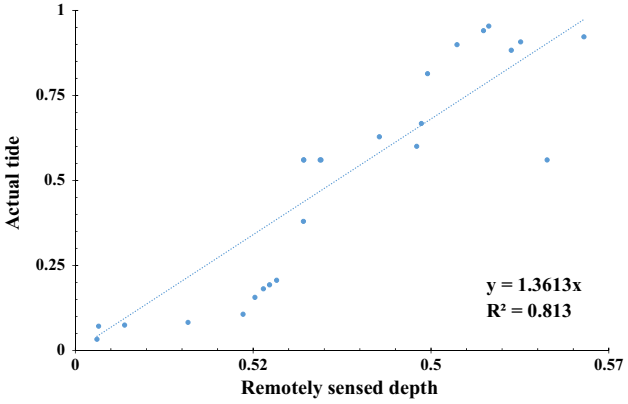

Figure 11: The correlation coefficient of the normalized minimum values (estimated/actual).

DII and the wind speed during April, similar to January. The correlation coefficient R^2 is 0.62.

The DII values of July range between 0 and 6, while the wind speed values (m/s) range between 0.1 and 6.7 m/s (Figure 16) with an average of 2.9 m/s during July. The highest value of the DII (6.2) corresponds to a wind speed of about 1 m/s. Similar to the April month, there is no clear trend of such a positive correlation between the DII and the wind speed during July in which the correlation coefficient R^2 is 0.28.

The DII values during October range between 0 and 1.3, while the wind speed values (m/s) range between 0.1 and 3 m/s with an average of 2.0 m/s. The highest value of the DII (1.3) corresponds to a wind speed of about 3 m/s. Similar to April and July, there is no clear trend of such a positive correlation between the DII and the wind speed during October in which the correlation coefficient R^2 is 0.33 (Figure 17).

The Bathymetry algorithm was developed and validated by ESA to monitor the majority of the world's

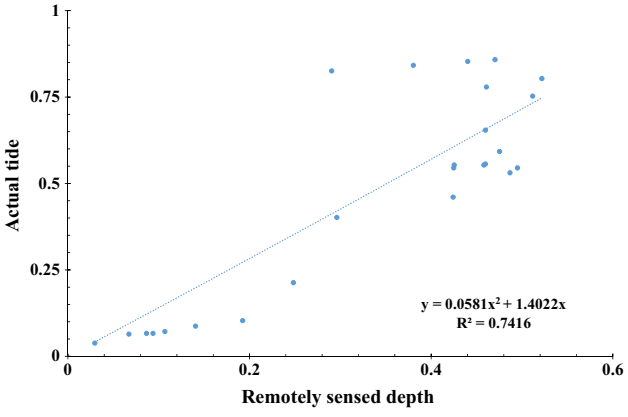

Figure 12: The correlation coefficient of the normalized maximum values (estimated/actual).

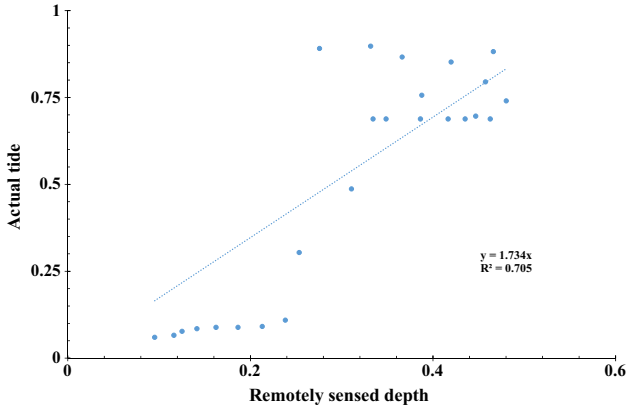

Figure 13: The correlation coefficient of the normalized mean values (estimated/actual).

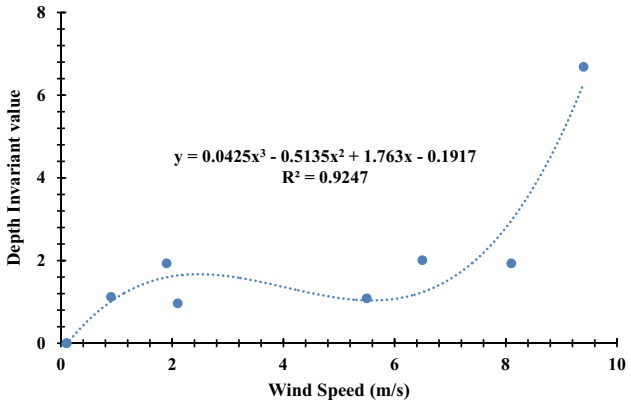

Figure 14: The DII versus wind speed (m/s) in January.

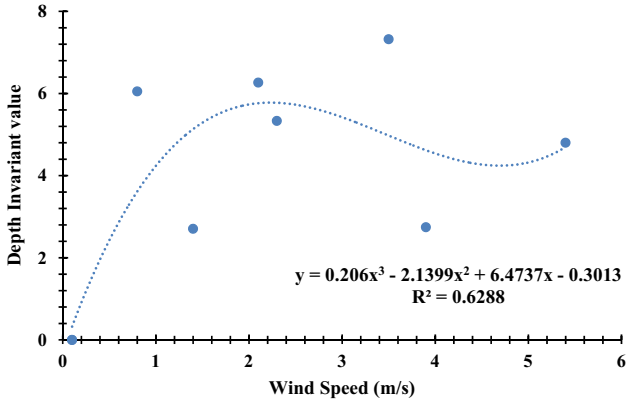

Figure 15: The DII versus wind speed (m/s) in April.

shallow water variations with the increased temporal and spatial resolution, and the validation process was conducted by several scholarly works of Spitzer and Dirks [20] and Poursanidis et al. [70]. Shallow water monitoring is very important because it appears to be the first

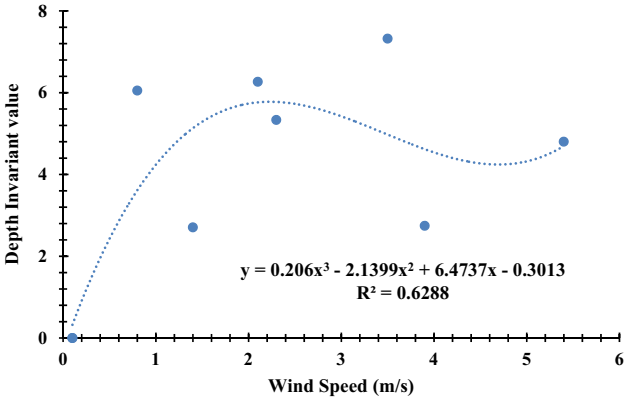

Figure 16: The DII versus wind speed (m/s) in April.

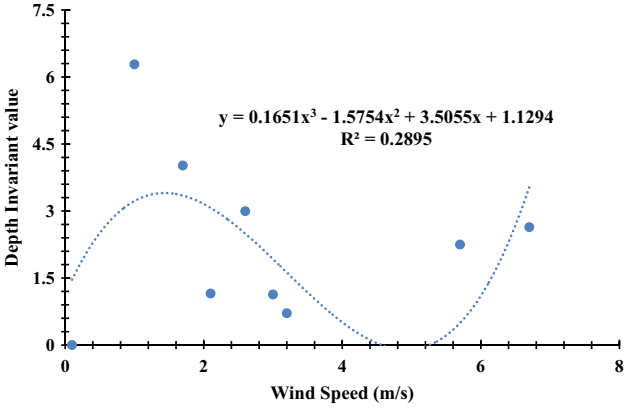

Figure 17: The DII versus wind speed (m/s) in October.

respondent to global climate changes, such as increased sea surface temperature, ultraviolet radiation, and acidification of seawater that results from higher levels of atmospheric CO_2 concentration [78–80].

Changes in winds and barometric pressures also cause variations in the tide level. In general, with low barometric pressure, the heights of both high and low water surfaces will be higher than predicted, while with high pressure, they will be lower than predicted [81]. There are also seasonal variations due to lower summer and higher winter atmospheric pressure. During summer, there is a regional "thermal low" pressure system over the Arabian Peninsula. These variations in pressure systems have been included in the predictions. Sea level change due to meteorological conditions is roughly a 1 cm rise or fall for every 1 millibar change in pressure [82,83].

According to Pugh [84], there are four classifications of tidal patterns or tide types based on the tide curve frequency and successive range variations: diurnal, semi-diurnal, mixed (mostly diurnal), and mixed (mostly semi-diurnal). For example, semi-diurnal tides have two high

and two low tides each day. The tidal day cycle requires 24 h and 50 min, since the moon, which exerts the greatest tidal influence, advances 50 min each day in its orbit around the Earth [85].

Tides occur twice daily, and the amplitude of the associated sea-level change differs from region to region. The rise and fall of the sea level associated with the fluctuations of tides produce tidal currents. Tidal currents, consequently, play a significant role in the coastline morphology and benthic depositional environments [86]. Tidal currents and waves are interlinked when it comes to coastlines accretion and erosions [86,87] although our information about the progress of the action of both tidal currents and waves on shoreline remains unexplored. During spring tide, wide tropical areas are submerged, while during neap tide tropical mudflats are exposed [86,88].

The overall range of the tide also changes daily. This effect is mainly caused by the changing alignment of the Earth, Sun, and Moon [89]. The minimum range tides (also called neap tides) occur at the quarter phases of the moon, while the maximum range tides (spring tides) occur during the full and new moon phases. Due to inertial effects, spring and neap tides can lag a couple of days behind the corresponding phases of the moon [90,91]. There is also a marked seasonal change in the tidal range. Maximum ranges, with the highest high tides and lowest low tides, generally occur near the summer and winter solstices (in June and December) when the sun is furthest from the Earth. However, local factors may cause considerable lag depending on the station location [92,93].

The force of "wind stress" and tidal actions are the major controller in the hydrographical features and general water circulation of the lagoon [46,50]. Tidal action is the major factor in shoreline erosion that led coastal cities to stronger exposure to tides [94,95]. The city has suffered from shoreline destruction because of the invasive tidal action powered principally by the wind speed and the direction over shallow waters [87,96]. The mean bathymetrical water depth of Al-Kharrar lagoon is 5 ± 2.8 m [45]. The interaction between the open water and the shallow water of Al-Kharrar lagoon occurs via a slightly wide and deeper inlet of 120 m width and 18 m water depth [45].

4 Conclusions and recommendations

Both the DII and astronomical tide reveal oscillation over four seasons and are positively correlated with the timeframe of the current study. The comparison between the DII and the astronomical tide is crossing each other between September 2017 and July 2018 when the DII is higher than the astronomical tide (cm). The DII against the wind speed (m/s) in the four seasons shows a positive correlation in January, but a weak correlation in April, July, and October. Higher wind speed (m/s) corresponds to higher values of the DII in January, while there is no clear pattern in April, July, and October. The images showed valid values over shallow areas where the solar radiation can penetrate the seafloor and is reflected from the features of interest, while over deep areas only noise values can be seen. Collectively, this processor is very useful in coral reef detection and inspection, which showed very competent use of remote sensing. It also explores the ways to work for water resources by using band variations techniques.

Acknowledgments: This project was funded by the Deanship of Scientific Research (DSR), King Abdulaziz University, Jeddah (Grant No. G-90-155-1441). The authors, therefore, acknowledge with thanks DSR technical and financial support.

References

[1] Tuia D, Volpi M, Copa L, Kanevski M, Munoz-Mari J. A survey of active learning algorithms for supervised remote sensing image classification. IEEE J Sel Top Signal Proc. 2011;5(3):606–17.
[2] Kennedy RE, Townsend PA, Gross JE, Cohen WB, Bolstad P, Wang YQ, et al. Remote sensing change detection tools for natural resource managers: understanding concepts and tradeoffs in the design of landscape monitoring projects. Remote Sens Environ. 2009;113(7):1382–96.
[3] Al Mamun A. Identification and monitoring the change of land use pattern using remote sensing and GIS: a case study of Dhaka city. IOSR J Mech Civ Eng. 2013;6(2):20–8.
[4] Bahrawi J, Elhag M. Consideration of seasonal variations of water radiometric indices for the estimation of soil moisture content in arid environment in saudi arabia. Appl Ecol Environ Res. 2019;17(1):285–303.
[5] Erbek FS, Özkan C, Taberner M. Comparison of maximum likelihood classification method with supervised artificial neural network algorithms for land use activities. Int J Remote Sens. 2004;25(9):1733–48.
[6] Elhag M. Detection of temporal changes of eastern coast of Saudi Arabia for better natural resources management. Indian J Geo-Mar Sci. 2016;45(1):29–37.
[7] Crippen RE. Calculating the vegetation index faster. Remote Sens Environ. 1990;34(1):71–3.
[8] Myneni RB, Hall FG, Sellers PJ, Marshak AL. The interpretation of spectral vegetation indexes. IEEE Trans Geosci Remote Sens. 1995;33(2):481–6.

[9] Elmore AJ, Mustard JF, Manning SJ, Lobell DB. Quantifying vegetation change in semiarid environments: precision and accuracy of spectral mixture analysis and the normalized difference vegetation index. Remote Sens Environ. 2000;73(1):87–102.
[10] Elhag M. Remotely sensed vegetation indices and spatial decision support system for better water consumption Regime in Nile Delta. A case study for rice cultivation suitability map. Life Sci J. 2014;11(1):201–9.
[11] Joyce KE, Belliss SE, Samsonov SV, McNeill SJ, Glassey PJ. A review of the status of satellite remote sensing and image processing techniques for mapping natural hazards and disasters. Prog Phys Geogr. 2009;33(2):183–207.
[12] Poursanidis D, Chrysoulakis N. Remote Sensing, natural hazards and the contribution of ESA sentinels missions. Remote Sens Appl Soc Environ. 2017;6:25–38.
[13] Wang Z, Xia J, Wang L, Mao Z, Zeng Q, Tian L, et al. Atmospheric correction methods for GF-1 WFV1 data in hazy weather. J Indian Soc Remote Sens. 2018;46(3):355–66.
[14] Shirvany R, Chabert M, Tourneret JY. Ship and oil-spill detection using the degree of polarization in linear and hybrid/compact dual-pol SAR. IEEE J Sel Top Appl Earth Obs Remote Sens. 2012;5(3):885–92.
[15] Grover A, Kumar S, Kumar A. Ship detection using Sentinel-1 SAR data. ISPRS Ann Photogramm Remote Sens Spat Inf Sci. 2018;4:5–324.
[16] Lanari R, Fornaro G, Riccio D, Migliaccio M, Papathanassiou KP, Moreira JR, et al. Generation of digital elevation models by using SIR-C/X-SAR multifrequency two-pass interferometry: The Etna case study. IEEE Trans Geosci Remote Sens. 1996;34(5):1097–114.
[17] Yang B, Xu H, Liu W, You Y, Xie X. Realistic lower bound on elevation estimation for tomographic SAR. IEEE J Sel Top Appl Earth Obs Remote Sens. 2018;11(7):2429–39.
[18] Shinozuka M, Ghanem R, Houshmand B, Mansouri B. Damage detection in urban areas by SAR imagery. J Eng Mech. 2000;126(7):769–77.
[19] Washaya P, Balz T. SAR coherence change detection of urban areas affected by disasters using sentinel-1 imagery. ISPRS Int Arch Photogramm Remote Sens Spat Inf Sci. 2018;XLII-3:1857–61.
[20] Spitzer D, Dirks RJ. Shallow water bathymetry and bottom classification by means of the Landsat and SPOT optical scanners. Earth remote sensing using the landsat thermatic mapper and SPOT sensor systems. Innsbruck, Austria: International Society for Optics and Photonics; 1986.
[21] de O Falcão A. Control of an oscillating-water-column wave power plant for maximum energy production. Appl Ocean Res. 2002;24(2):73–82.
[22] McKinna LIW, Fearns PRC, Weeks SJ, Werdell PJ, Reichstetter M, Franz BA, et al. A semianalytical ocean color inversion algorithm with explicit water column depth and substrate reflectance parameterization. J Geophys Res Ocean. 2015;120(3):1741–70.
[23] Gerling T. Structure of the surface wind field from the Seasat SAR. J Geophys Res Ocean. 1986;91(C2):2308–20.
[24] Yang X, Li X, Zheng Q, Gu X, Pichel WG, Li Z. Comparison of ocean-surface winds retrieved from QuikSCAT scatterometer and Radarsat-1 SAR in offshore waters of the US west coast. IEEE Geosci Remote Sens Lett. 2010;8(1):163–7.
[25] Ballard S, Graber H, Caruso M. Coastal surface wind measurements derived from SAR. 2017 IEEE international geoscience and remote sensing symposium (IGARSS). Fort Worth, TX, USA: IEEE; 2017.
[26] Chelton DB, Enfield DB. Ocean signals in tide gauge records. J Geophys Res Solid Earth. 1986;91(B9):9081–98.
[27] Idier D, Bertin X, Thompson P, Pickering MD. Interactions between mean sea level, tide, surge, waves and flooding: mechanisms and contributions to sea level variations at the coast. Surv Geophys. 2019;40(6):1603–30.
[28] Münchow A, Melling H. Ocean current observations from Nares Strait to the west of Greenland: interannual to tidal variability and forcing. J Mar Res. 2008;66(6):801–33.
[29] Goward Brown AJ, Lewis M, Barton BI, Jeans G, Spall SA. Investigation of the modulation of the tidal stream resource by ocean currents through a complex tidal channel. J Mar Sci Eng. 2019;7(10):341.
[30] Platt T. Primary production of the ocean water column as a function of surface light intensity: algorithms for remote sensing. Deep Sea Res Part A Oceanogr Res Pap. 1986;33(2):149–63.
[31] Stumpf RP, Holderied K, Sinclair M. Determination of water depth with high-resolution satellite imagery over variable bottom types. Limnol Oceanogr. 2003;48(1part2):547–56.
[32] Kerr JM, Purkis S. An algorithm for optically-deriving water depth from multispectral imagery in coral reef landscapes in the absence of ground-truth data. Remote Sens Environ. 2018;210:307–24.
[33] Li J, Ma R, Xue K, Zhang Y, Loiselle S. A remote sensing algorithm of column-integrated algal biomass covering algal bloom conditions in a shallow Eutrophic Lake. ISPRS Int J Geo-Inf. 2018;7(12):466.
[34] Chen B, Yang Y, Xu D, Huang E. A dual band algorithm for shallow water depth retrieval from high spatial resolution imagery with no ground truth. ISPRS J Photogramm Remote Sens. 2019;151:1–13.
[35] Lyzenga DR. Passive remote sensing techniques for mapping water depth and bottom features. Appl Opt. 1978;17(3):379–83.
[36] Siregar V, Agus SB, Subarno T, Prabowo NW. Mapping shallow waters habitats using OBIA by applying several approaches of depth invariant index in North Kepulauan Seribu. IOP Conf Ser Earth Environ Sci. 2018;149:012052.
[37] Eugenio F, Marcello J, Martin J. High-resolution maps of bathymetry and benthic habitats in shallow-water environments using multispectral remote sensing imagery. IEEE Trans Geosci Remote Sens. 2015;53(7):3539–49.
[38] Hedley JD, Roelfsema C, Brando V, Giardino C, Kutser T, Phinn S, et al. Coral reef applications of Sentinel-2: coverage, characteristics, bathymetry and benthic mapping with comparison to Landsat 8. Remote Sens Environ. 2018;216:598–614.
[39] Anis A, Moum J. Surface wave–turbulence interactions. Scaling $\varepsilon(z)$ near the sea surface. J Phys Oceanogr. 1995;25(9):2025–45.
[40] Lee JA, Hacker JP, Delle Monache L, Kosović B, Clifton A, Vandenberghe F, et al. Improving wind predictions in the marine atmospheric boundary layer through parameter estimation in a single-column model. Mon Weather Rev. 2017;145(1):5–24.

[41] Laxague NJM, Haus BK, Ortiz-Suslow DG, Smith CJ, Novelli G, Dai H, et al. Passive optical sensing of the near-surface wind-driven current profile. J Atmos Ocean Technol. 2017;34(5):1097–111.
[42] Almazroui M, Ammar K, Islam MN, Awad AM, Khalid MS. Spring Saharan cyclones over Saudi Arabia: preliminary study of the impacts on climate. Earth Syst Environ. 2019;3(2):153–71.
[43] Loizeau J-L, Dominik J, Luzzi T, Vernet JP. Sediment core correlation and mapping of sediment accumulation rates in Lake Geneva (Switzerland, France) using volume magnetic susceptibility. J Great Lakes Res. 1997;23(4):391–402.
[44] Gaber A, Soliman F, Koch M, El-Baz F. Using full-polarimetric SAR data to characterize the surface sediments in desert areas: a case study in El-Gallaba Plain, Egypt. Remote Sens Environ. 2015;162:11–28.
[45] Al-Dubai TA, Abu-Zied RH, Basaham AS. Present environmental status of Al-Kharrar Lagoon, central of the eastern Red Sea coast, Saudi Arabia. Arab J Geosci. 2017;10(14):305.
[46] Al-Barakat A. Some hydrographic features of Rabigh lagoon along the eastern coast of the Red Sea. Mar Sci. 2010;21:1–132.
[47] Al-Washmi H. Sedimentological aspects and environmental conditions recognized from the bottom sediments of Al-Kharrar Lagoon, eastern Red Sea coastal plain, Saudi Arabia. J KAU Mar Sci. 1999;10:71–87.
[48] Zhao B, Wang Z, Chen J, Chen Z. Marine sediment records and relative sea level change during late Pleistocene in the Changjiang delta area and adjacent continental shelf. Quaternary Int. 2008;186(1):164–72.
[49] Bahrawi JA, Elhag M. Simulation of Sea level rise and its impacts on the western coastal area of Saudi Arabia. Indian J Geo-Mar Sci. 2016;45(1):54–61.
[50] Elhag M, Bahrawi JA. Sedimentation mapping in shallow shoreline of arid environments using active remote sensing data. Nat Hazards. 2019;99(2):879–94.
[51] Mori N, Shimura T, Yasuda T, Mase H. Multi-model climate projections of ocean surface variables under different climate scenarios – future change of waves, sea level and wind. Ocean Eng. 2013;71:122–9.
[52] Sibanda M, Mutanga O, Rouget M. Examining the potential of Sentinel-2 MSI spectral resolution in quantifying above ground biomass across different fertilizer treatments. ISPRS J Photogramm Remote Sens. 2015;110:55–65.
[53] Pahlevan N, Sarkar S, Franz BA, Balasubramanian SV, He J. Sentinel-2 multispectral instrument (MSI) data processing for aquatic science applications: Demonstrations and validations. Remote Sens Environ. 2017;201:47–56.
[54] Du Y, Teillet PM, Cihlar J. Radiometric normalization of multitemporal high-resolution satellite images with quality control for land cover change detection. Remote Sens Environ. 2002;82(1):123–34.
[55] Zhang Y, Yu L, Sun M, Zhu X. A mixed radiometric normalization method for mosaicking of high-resolution satellite imagery. IEEE Trans Geosci Remote Sens. 2017;55(5):2972–84.
[56] Schott JR, Salvaggio C, Volchok WJ. Radiometric scene normalization using pseudoinvariant features. Remote Sens Environ. 1988;26(1):1–16.
[57] Sadeghi V, Ahmadi FF, Ebadi H. A new automatic regression-based approach for relative radiometric normalization of multitemporal satellite imagery. Comput Appl Math. 2017;36(2):825–42.
[58] Jia L, Su Z, van den Hurk B, Menenti M, Moene A, De Bruin HAR, et al. Estimation of sensible heat flux using the surface energy balance system (SEBS) and ATSR measurements. Phys Chem Earth Parts A/B/C. 2003;28(1–3):75–88.
[59] Cho K, Kim Y. Simulation of Sentinel-2 product using airborne hyperspectral image and analysis of TOA and BOA reflectance for evaluation of Sen2cor atmosphere correction: Focused on agricultural land. Korean J Remote Sens. 2019;35(2):251–63.
[60] Louis J, Debaecker V, Pflug B, Main-Knorn M, Bieniarz J, Mueller-Wilm U, et al. Sentinel-2 sen2cor: L2a processor for users. Proceedings of the living planet symposium, Prague. Prague: Czech Republic; 2016.
[61] Main-Knorn M, Pflug B, Louis J, Debaecker V. Sen2Cor for sentinel-2. Image and Signal Processing for Remote Sensing XXIII. Warsaw, Poland: International Society for Optics and Photonics; 2017.
[62] Su H, Liu H, Heyman WD. Automated derivation of bathymetric information from multi-spectral satellite imagery using a non-linear inversion model. Mar Geodesy. 2008;31(4):281–98.
[63] Toole DA, Siegel DA, Menzies DW, Neumann MJ, Smith RC. Remote-sensing reflectance determinations in the coastal ocean environment: impact of instrumental characteristics and environmental variability. Appl Opt. 2000;39(3):456–69.
[64] Hochberg EJ, Andrefouet S, Tyler MR. Sea surface correction of high spatial resolution Ikonos images to improve bottom mapping in near-shore environments. IEEE Trans Geosci Remote Sens. 2003;41(7):1724–9.
[65] Hedley JD, Harborne AR, Mumby PJ. Simple and robust removal of sun glint for mapping shallow-water benthos. Int J Remote Sens. 2005;26(10):2107–12.
[66] Hedley J, Roelfsema C, Koetz B, Phinn S. Capability of the Sentinel 2 mission for tropical coral reef mapping and coral bleaching detection. Remote Sens Environ. 2012;120:145–55.
[67] Sordillo LA, Pu Y, Pratavieira S, Budansky Y, Alfano RR. Deep optical imaging of tissue using the second and third near-infrared spectral windows. J Biomed Opt. 2014;19(5):056004.
[68] Wicaksono P. Improving the accuracy of multispectral-based benthic habitats mapping using image rotations: The application of principle component analysis and independent component analysis. Eur J Remote Sens. 2016;49(1):433–63.
[69] Philpot WD. Bathymetric mapping with passive multispectral imagery. Appl Opt. 1989;28(8):1569–78.
[70] Poursanidis D, Traganos D, Reinartz P, Chrysoulakis N. On the use of Sentinel-2 for coastal habitat mapping and satellite-derived bathymetry estimation using downscaled coastal aerosol band. Int J Appl Earth Obs Geoinf. 2019;80:58–70.
[71] Nurlidiasari M, Budiman S. Mapping coral reef habitat with and without water column correction using Quickbird image. Int J Remote Sens Earth Sci. 2010;2:2.
[72] Kim S-H, Yang CS, Ouchi K. Validation of the semi-analytical algorithm for estimating vertical underwater visibility using MODIS data in the waters around Korea. Korean J Remote Sens. 2013;29(6):601–10.
[73] Lehner S, Schulz-Stellenfleth J, Schattler B, Breit H, Horstmann J. Wind and wave measurements using complex ERS-2 SAR wave mode data. IEEE Trans Geosci Remote Sens. 2000;38(5):2246–57.

[74] Yijun He H, Perrie W, Qingping Zou, Vachon PW. A new wind vector algorithm for C-band SAR. IEEE Trans Geosci Remote Sens. 2005;43(7):1453–8.
[75] Stoffelen A, Anderson D. Scatterometer data interpretation: estimation and validation of the transfer function CMOD4. J Geophys Res Ocean. 1997;102(C3):5767–80.
[76] Park J-W, Korosov A, Babiker M, Sandven S. Efficient thermal noise removal of Sentinel-1 image and its impacts on sea ice applications. Vienna, Austria: EGU general assembly conference abstracts; 2017.
[77] Ali I, Cao S, Naeimi V, Paulik C, Wagner W. Methods to remove the border noise from Sentinel-1 synthetic aperture radar data: implications and importance for time-series analysis. IEEE J Sel Top Appl Earth Obs Remote Sens. 2018;11(3):777–86.
[78] Löptien U, Meier HM. The influence of increasing water turbidity on the sea surface temperature in the Baltic Sea: a model sensitivity study. J Mar Syst. 2011;88(2):323–31.
[79] Barnes BB, Hu C, Cannizzaro JP, Craig SE, Hallock P, Jones DL, et al. Estimation of diffuse attenuation of ultraviolet light in optically shallow Florida keys waters from MODIS measurements. Remote Sens Environ. 2014;140:519–32.
[80] Melzner F, Mark FC, Seibel BA, Tomanek L. Ocean acidification and coastal marine invertebrates: Tracking CO2 effects from seawater to the cell. Annu Rev Mar Sci. 2019;12.
[81] Rezanejad K, Guedes Soares C, López I, Carballo R. Experimental and numerical investigation of the hydrodynamic performance of an oscillating water column wave energy converter. Renewable Energy. 2017;106:1–16.
[82] Miller L, Douglas BC. Gyre-scale atmospheric pressure variations and their relation to 19th and 20th century sea level rise. Geophys Res Lett. 2007;34:16.
[83] Woodworth PL, Melet A, Marcos M, Ray RD, Wöppelmann G, Sasaki YN, et al. Forcing factors affecting sea level changes at the coast. Surv Geophys. 2019;40(6):1351–97.
[84] Pugh D. Changing sea levels: Effects of tides, weather and climate. Cambridge: Cambridge University Press; 2004.
[85] Foster RG, Roenneberg T. Human responses to the geophysical daily, annual and lunar cycles. Curr Biol. 2008;18(17):R784–94.
[86] Shi B, Cooper JR, Pratolongo PD, Gao S, Bouma TJ, Li G, et al. Erosion and accretion on a mudflat: the importance of very shallow-water effects. J Geophys Res Ocean. 2017;122(12):9476–99.
[87] Lafta AA, Altaei SA, Al-Hashimi NH. Impacts of potential sea-level rise on tidal dynamics in Khor Abdullah and Khor Al-Zubair, northwest of Arabian Gulf. Earth Syst Environ. 2020;4(1):93–105.
[88] Pratolongo PD, Perillo GME, Piccolo MC. Combined effects of waves and plants on a mud deposition event at a mudflat-saltmarsh edge in the Bahía Blanca estuary. Estuar Coast Shelf Sci. 2010;87(2):207–12.
[89] Guo H, Ding Y, Liu G, Zhang D, Fu W, Zhang L. Conceptual study of lunar-based SAR for global change monitoring. Sci China Earth Sci. 2014;57(8):1771–9.
[90] Shi W, Wang M, Jiang L. Spring-neap tidal effects on satellite ocean color observations in the Bohai Sea, Yellow Sea, and East China Sea. J Geophys Res Ocean. 2011;116(C12):C12032.
[91] Zhou Z, Bian C, Wang C, Jiang W, Bi R. Quantitative assessment on multiple timescale features and dynamics of sea surface suspended sediment concentration using remote sensing data. J Geophys Res Ocean. 2017;122(11):8739–52.
[92] Martino RL, Sanderson DD. Fourier and autocorrelation analysis of estuarine tidal rhythmites, lower Breathitt Formation (Pennsylvanian), eastern Kentucky, USA. J Sediment Res. 1993;63(1):105–19.
[93] Lacy JR, Ferner MC, Callaway JC. The influence of neap–spring tidal variation and wave energy on sediment flux in salt marsh tidal creeks. Earth Surf Proc Landf. 2018;43(11):2384–96.
[94] Lim M, Rosser NJ, Petley DN, Keen M. Quantifying the controls and influence of tide and wave impacts on coastal rock cliff erosion. J Coast Res. 2011;27(1):46–56.
[95] FitzGerald DM. Shoreline erosional-depositional processes associated with tidal inlets. Hydrodynamics and sediment dynamics of tidal inlets. New York: Springer; 1988. p. 186–225.
[96] Nasr D. Coral reefs of the Red Sea with special reference to the Sudanese coastal area. The Red Sea. Berlin: Springer; 2015. p. 453–69.